Gradients of Atmospheric Temperature and Humidity Controlled by Local Urban Land-Use Intensity in Boston

J. A. WANG, L. R. HUTYRA, D. LI, AND M. A. FRIEDL

Department of Earth and Environment, Boston University, Boston, Massachusetts

(Manuscript received 26 September 2016, in final form 22 November 2016)

ABSTRACT

Cities are home to the majority of humanity. Therefore, understanding the mechanisms that control urban climates has substantial societal importance to a variety of sectors, including public health and energy management. In this study, data from an urban sensor network (25 stations) and moderate-resolution remote sensing were used to explore how spatial variation in near-surface air temperature T_a, vapor pressure deficit (VPD), and land surface temperature (LST) depend on local variations in urban land use, both diurnally and seasonally, in the Boston, Massachusetts, metropolitan area. Positive correlations were observed between the amount of local impervious surface area (ISA) and both T_a and VPD. Heat-island effects peaked during the growing-season nighttime, when mean T_a and VPD increased by up to 0.02°C and 0.008 kPa, respectively, per unit ISA. Air temperature and VPD were strongly coupled, but their relationship exhibited significant diurnal hysteresis during the growing season, with changes in VPD generally preceding changes in T_a. Over 79% of the urban–rural difference in VPD was explained by differences in near-surface atmospheric water content, which the authors attribute to reduced evapotranspiration from lower canopy cover in Boston's urban core. Changes in daytime heat-island intensity were mediated by seasonal feedbacks between vegetation transpiration and VPD forcing. Differences between LST and T_a showed weaker coupling in highly urbanized areas than in rural areas, with summertime surface-urban-heat-island intensity (based on LST) being up to 14°C higher than corresponding urban–rural differences in T_a.

1. Introduction

Urban areas are expected to expand rapidly in the coming decades, particularly in small and midsized cities in the developing world (Seto et al. 2012). Because cities are home to the majority of Earth's population, changes in the near-surface climate of cities have important implications for human health and energy use, particularly as they enhance the magnitude of extreme events like heat waves (Li and Bou-Zeid 2013; Schatz and Kucharik 2015). In humid climates, urban development typically modifies surface energy and radiation budgets by displacing background vegetative cover, raising surface and air temperatures, and creating so-called urban heat islands (UHI) (Oke 1982; Arnfield 2003; Weng et al. 2004; Schatz and Kucharik 2014). During the day, UHIs are primarily caused by reduced evapotranspiration and changes in albedo relative to surrounding rural areas. At night, cities are warmer relative to nearby rural areas because built environments tend to have high thermal inertia; urban morphology (e.g., street canyons between buildings) traps outgoing longwave radiation; and waste heat from automobiles, buildings, and other anthropogenic activities provides a direct source of heat to the lower atmosphere (Oke 1982; Arnfield 2003; Hinkel and Nelson 2007; Stewart and Oke 2012). Because of complex interactions among surface properties and surface radiation and energy budgets, the magnitude of urban heating varies seasonally and diurnally, both within and across cities (Schatz and Kucharik 2014).

Studies of the UHI typically use point measurements of near-surface air temperature T_a or satelliteborne thermal remote sensing to characterize the nature and magnitude of urban–rural temperature differences. In this paper, we refer to UHI specifically in reference to elevated air temperature associated with urban land use, in contrast to the surface urban heat island (SUHI), which represents elevated urban land surface temperature. Remote sensing affords spatially explicit characterization of variability in the intensity of the SUHI, but these studies are often constrained by temporal sampling (i.e., overpass times, which are typically midmorning) and are limited in utility

Corresponding author e-mail: J. A. Wang, jonwang@bu.edu

DOI: 10.1175/JAMC-D-16-0325.1

© 2017 American Meteorological Society. For information regarding reuse of this content and general copyright information, consult the AMS Copyright Policy (www.ametsoc.org/PUBSReuseLicenses).

since land surface temperatures (LST) deviate substantially from near-surface air temperatures (Yuan and Bauer 2007; Zhou et al. 2013; Weng and Fu 2014). Despite these problems, LSTs are often used as surrogates for air temperatures (e.g., Zhang et al. 2004; Melaas et al. 2016) even though precise understanding of the coupling between LST and T_a is lacking (Oyler et al. 2016), potentially leading to biases in the interpretation and magnitude of urban–rural temperature differences in UHI studies. In contrast, studies of UHIs that use automated point sampling to measure T_a directly in order to characterize temporal structure (i.e., diurnal and seasonal variability) generally do not consider spatially explicit UHI representations, instead relying on measures of UHI magnitude that are based on bulk differences in T_a measurements between relatively few urban sites and nearby rural sites (e.g., Gedzelman et al. 2003; Kim and Baik 2005; Hinkel and Nelson 2007; Kolokotroni and Giridharan 2008; Yang et al. 2013).

A variety of recent studies have incorporated statistical modeling to spatially extrapolate sensor-network observations (e.g., Hjort et al. 2011; Schatz and Kucharik 2014), but more work is needed to better understand and characterize how land use and land cover control urban microclimate (Stewart and Oke 2012). For example, biophysically based classifications of subcity spatial units have been introduced in various studies to better differentiate UHI impacts at local, rather than regional, scales. Such local classifications exploit variations in urban morphology, land-cover types, and vegetation-cover dynamics and have included, among others, ''meteorologically significant land uses'' (Auer 1978), ''urban terrain zones'' (Ellefsen 1991), ''urban zones for characterizing energy partitioning'' (Loridan and Grimmond 2012), and ''local climate zones'' (Stewart and Oke 2012). By partitioning the urban landscape into physically meaningful units, these studies have sought to more precisely characterize the nonlinear interactions between observed UHIs and biophysical controls such as bioclimatic context (Imhoff et al. 2010; Hjort et al. 2011), local land use (Grossman-Clarke et al. 2010), and time of day and year (Eliasson and Svensson 2003; Gedzelman et al. 2003; Kolokotroni and Giridharan 2008; Yang et al. 2013; Zhou et al. 2013, Bounoua et al. 2015). Despite these efforts, however, UHI studies still lack a generalizable and widely used classification system for describing local urban climate zones.

In addition to warming, there is considerable evidence that urban land use modifies local humidity (Hage 1975; Lee 1991; Jáuregui and Tejeda 1997; Unger 1999). Similar to studies of urban–rural differences in air temperature, studies of urban–rural differences in humidity also typically focus on bulk differences between urban and rural sensors (Hage 1975; Lee 1991; Jáuregui and Tejeda 1997; Unger 1999). Because humidity is an important control on urban heat indices and urban ecological processes, understanding the processes behind changes in urban humidity is important for UHI mitigation strategies (Bowler et al. 2010; Onishi et al. 2010; Georgescu et al. 2014; Li et al. 2014), for management of ecosystem services provided by urban forests (Nowak 2006; Raciti et al. 2012; Briber et al. 2015), and for understanding how sensible and latent heat fluxes are partitioned in cities (Oke 1982; Masson 2000). Studies of urban–rural differences in humidity vary significantly in their findings, with some studies identifying an urban moisture excess (Unger 1999; Unkašević et al. 2001; Kuttler et al. 2007) and other studies demonstrating marked urban drying (Ackerman 1987). Most studies reveal a strong dependence of urban humidity on the season and time of day (e.g., cities that are relatively dry during the summer daytime and relatively moist during the winter nighttime), although the feedbacks and processes are rarely explored (Hage 1975; Lee 1991; Jáuregui and Tejeda 1997; Deosthali 2000). Most important, there remains considerable uncertainty in the spatial and temporal structure and mechanisms that give rise to urban–rural differences in near-surface atmospheric moisture, particularly in relation to differences in temperature. Warmer temperatures can decrease relative humidity in urban areas, but urban humidity differences can also be driven by differences in absolute humidity.

In this study, we used data from an in situ sensor network and remote sensing in Boston, Massachusetts, to investigate the degree to which spatial heterogeneity in urban land-use intensity controls local perturbations in air temperature, skin temperature, and local humidity relative to the background surface climate. We focus on impervious surface area (ISA), a quantitative, continuously varying land-cover property and the principal land-cover modification associated with urbanization. ISA has been used widely to study the SUHI via remote sensing (Yuan and Bauer 2007; Weng and Fu 2014; Zhou et al. 2013) and has recently been shown to be correlated with air temperatures (Schatz and Kucharik 2014). Many studies have shown that surface climate is dependent on the local vegetative cover; changes in vegetative cover are only indirectly related to urbanization, however, and the relationship between remote sensing–based estimates of land surface greenness (i.e., vegetation indices) and urban land use is complex and is variable in space. In contrast, ISA is a clearly defined, static, and physically interpretable property. Here, we investigate how local variations in ISA mediate dynamics in the local urban surface climate, focusing on the time-varying impacts of urbanization on three microclimatic

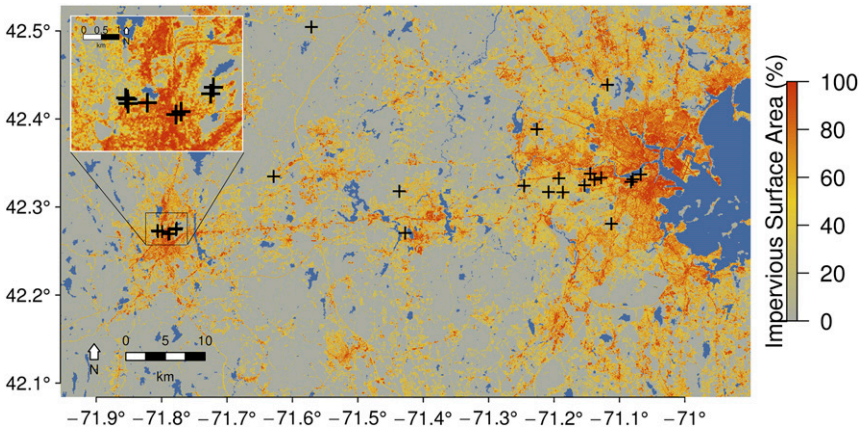

FIG. 1. Map of study area in Boston, including National Land Cover Database 2011 percent of ISA coverage and locations of HOBO U23 air temperature–RH sensors as plus signs. The inset shows a close-up of Worcester, where a denser set of sensors was set up in Worcester's urban core and urban forests.

variables: LST, T_a, and vapor pressure deficit (VPD). We specifically aim to address the following questions: 1) How does local urban land-use intensity (ISA) influence seasonal and diurnal variations in urban atmospheric temperature and humidity? 2) To what degree are observed differences in urban–rural humidity driven by changes in atmospheric water content versus changes in urban air temperatures? 3) What are the major differences in land surface temperature versus surface air temperature and what are the resulting differences in SUHIs versus UHIs that are based on air temperature?

2. Data and methods

a. Study region, sensor network, and ancillary data

The study region covers the cities of Boston and Worcester, Massachusetts (Fig. 1), covering 4292 km^2 of urban land use, coastal wetlands, and hardwood forests over an elevation range from 0 to 192 m MSL. The climate exhibits considerable seasonality in temperature but relatively uniform precipitation. Deciduous vegetation phenology is primarily controlled by temperature (e.g., Richardson et al. 2006; Friedl et al. 2014), with green leaves typically developing in early or mid-May and senescing in mid-October. The UHI can advance the start of season by up to two weeks and delay the end of season by over a week in urban areas relative to rural areas (Zhang et al. 2004; Melaas et al. 2016), suggesting a possible feedback between UHI effects and green-leaf phenology.

The T_a and relative humidity (RH) measurements were collected at 15-min intervals between March 2014 and November 2015 at 25 sites that spanned an urban-to-rural gradient around Boston (Fig. 1). The measurements were then used to calculate VPD for each observation pair. Temperature and humidity sensors (Onset Computer Corp. HOBO U23-001) were housed in radiation shields and mounted on trees at approximately 2-m height above the ground. To ensure that the radiation shields effectively eliminated radiative heating, we installed one sensor with no canopy shading adjacent to an actively aspirated temperature sensor at the Harvard Forest. Comparison of temperature time series from the HOBO and aspirated sensors showed no significant differences (data not shown), suggesting that the HOBO data were representative of atmospheric conditions. For this analysis, we aggregated the 15-min observations into means over 1-h time steps.

To complement the in situ air temperature and humidity observations, we incorporated several auxiliary remote sensing datasets into our analysis. We used the National Land Cover Database ISA 30-m product to characterize the proportion of area surrounding each site that was converted to impervious land (Homer et al. 2015). We used data from the Shuttle Radar Topography Mission, version 2, product (1 arc s) to characterize elevation at 90-m spatial resolution throughout our study region (USGS 2004). To estimate the timing of green-leaf emergence and senescence at each of our sites, we used results from the Landsat phenology algorithm, which exploits dense time series of Landsat images of land surface greenness to estimate start of season ("leaf-out") and end of season (senescence) dates for vegetation at each of our sites (Melaas et al. 2013). We extracted ISA, elevation, and phenological data for all pixels located within fixed buffers of each of our HOBO sensors [see section 2b(1)]. Sensors were located in a variety of land-cover types, including open

grass, low-density residential urban, high-density residential urban, commercial/industrial urban, and forest, and were distributed across the range of elevation and ISA in our region (Fig. 1). In addition, we used brightness temperature and surface reflectance from Landsat images coinciding with our sensor-network observational period to analyze the difference between land surface temperature and surface air temperature in our study area.

b. Analysis

1) Linear models of T_A and VPD vs ISA

For each hourly observation, we calculated multiple-linear-regression models predicting T_a and VPD as a function of local elevation, proximity to the ocean, and local ISA to characterize the time-dependent relationship between surface climate and local urban land-use intensity. We recorded 14 214 observations at each of 25 sites, for 355 350 total site hours, and we used the Akaike information criterion to select the set of predictor variables. Distance from the ocean was included to account for the effect of large water bodies on UHI intensities (cf. Eliasson and Svensson 2003; Alcoforado and Andrade 2006; Hjort et al. 2011; Schatz and Kucharik 2014). We assumed that the impact of smaller water bodies was negligible. Each hourly time step was modeled separately, with no a priori assumptions about the structure of the diurnal variation or seasonality of Boston's UHI.

The estimated regression models were used to measure the UHI intensity at each time step. We refer to a unit change in ISA as corresponding to a change in ISA of 1%. UHI intensity was defined as the change in T_a or VPD per unit ISA [i.e., $\partial T_a/\partial$(ISA) (°C per 1%) and ∂(VPD)/∂(ISA) (kPa per 1%)], which is equivalent to the slope coefficient for ISA in the multiple-regression models. Hereinafter, we refer to these marginal impacts as "∂T_a" and "∂VPD," which represent the sensitivity of air temperature or vapor pressure deficit to local ISA. While T_a and VPD were modeled using all of our predictor variables, we isolate the effect of ISA from controls imposed by elevation and water effects by focusing on ∂T_a and ∂VPD. A similar method was used in Schatz and Kucharik (2014, 2015), although they define intensity by the maximum potential effect rather than the marginal effect (i.e., the difference between their model prediction at ISA = 100% and their model prediction at ISA = 0%). For the entire study period, this yielded a total of 14 213 estimated models for each of temperature and VPD.

To determine the range of spatial influence of ISA on T_a and VPD in our study area, we tested 10 buffer sizes ranging from 50 to 1000 m surrounding each sensor. The average correlation coefficient squared (R^2) for both T_a and VPD was highest at a buffer size of 300 m, with the R^2 for air temperature averaging 0.67 and the R^2 for VPD averaging 0.60. Therefore, our linear models use the area-averaged impervious surface area and elevation in 300-m radii surrounding each sensor. This buffer size is similar in magnitude to the average spatial fetches of sensors determined by Oke (2006), who found an optimal buffer of 500 m, by Hjort et al. (2011), who found an optimal buffer radius of 400 m, by Schatz and Kucharik (2014), who found an optimal buffer radius between 455 and 536 m, and by Hjort et al. (2016), who analyzed spatial correlations to find optimal buffer radii for urban land use ranging from 100 to 300 m.

2) Attribution of urban dryness

Urban–rural differences in VPD can be caused by differences in temperature or by differences in the water vapor content of the atmosphere. To quantify the relative contributions of urban-induced changes in temperature versus humidity on the VPD gradient, we estimated the relative contributions of each following the method described by Diao et al. (2014):

$$\mathrm{VPD} = (1 - \mathrm{RH})e_s,$$

$$\partial\mathrm{VPD}_{\mathrm{Ta}} = \frac{\partial \mathrm{VPD}}{\partial e_s}\partial e_s = (1 - \mathrm{RH})\partial e_s, \quad \text{and}$$

$$\partial\mathrm{VPD}_q = \frac{\partial \mathrm{VPD}}{\partial \mathrm{RH}}\partial\mathrm{RH} = -e_s\partial\mathrm{RH},$$

where e_s is the saturation vapor pressure, $\partial\mathrm{VPD}_{\mathrm{Ta}}$ is the change in vapor pressure deficit attributable to changes in temperature (via changes in e_s), and $\partial\mathrm{VP}D_q$ is the change in VPD attributable to changes in relative humidity. The sum of $\partial\mathrm{VPD}_q$ and $\partial\mathrm{VPD}_{\mathrm{Ta}}$ is the total observed change in VPD. The ∂RH and ∂e_s are the urban–rural differences in RH and e_s, respectively, estimated at 1-h time steps using linear models similar to those described above for T_a and VPD.

3) Spatiotemporal variability in net urban heating and urban drying

We mapped spatiotemporal variability in T_a and VPD caused by urbanization (ΔT_a and ΔVPD) by multiplying the map of ISA with ∂T_a and ∂VPD from the linear models. We analyze averaged values of ∂T_a and ∂VPD representing summer daytime (1000 LT June–August), summer nighttime (0000 LT June–August), spring daytime (1000 LT March–May), and spring nighttime (0000 LT March–May). These ΔT_a and ΔVPD maps represent the total observed UHI effect for the given time periods. The 1000 LT time point was chosen for daytime effects to roughly match the overpass time of Landsat (~1015 LT), which we use to calculate SUHI. To be consistent with the linear models that we estimated using the sensor

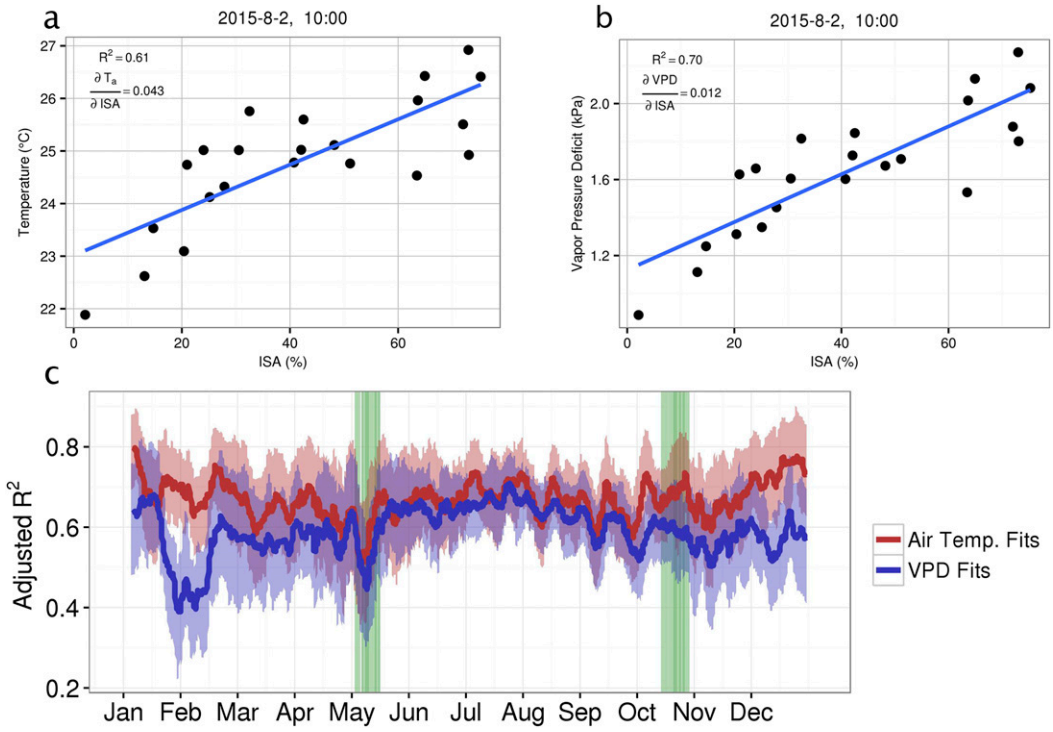

FIG. 2. (a) Example linear relationship between air temperature and ISA ($R^2 = 0.61$; $\partial T_a = 0.043$°C per unit ISA) across all sensors for 1000 LT 2 Aug 2015. (b) Example linear relationship between VPD and ISA ($R^2 = 0.70$; ∂VPD = 0.012 kPa per unit ISA) across all sensors for 1000 LT 2 Aug 2015. (c) The 30-day running average for the R^2 of the model fits; shaded areas show ±2 std dev. The vertical green bars indicate the timing of vegetation phenology (leaf-out and senescence) across sensors in network.

data, we upscaled the 30-m ISA data using a moving window to compute the average ISA in 300-m buffers surrounding each ISA grid cell.

4) MAPPING SUHI USING LANDSAT

The Landsat series of satellites measures emission of thermal radiation, providing top-of-atmosphere brightness temperatures. These data were cloud screened using the "fmask" algorithm for detection of clouds and cloud shadows (Zhu and Woodcock 2012) and then converted to LST by correcting the top-of-atmosphere brightness temperatures for atmospheric absorption and scattering using a Landsat-specific tool based on the "MODTRAN5" radiative transfer model (Barsi et al. 2005; http://atmcorr.gsfc.nasa.gov). Thermal emissivity at each pixel was prescribed on the basis of an area-weighted average of subpixel emissivities as in Sobrino et al. (2004). To reduce noise and avoid issues related to missing data from clouds, we calculated the average LST during summer (July–August; growing season) and spring (March–May; nongrowing season) at each pixel over the 2000–15 Landsat record for our study region. The date range accommodates the availability of atmospheric correction data from the MODTRAN5 model. We thus produced maps of cloud-screened seasonal averages of land surface temperatures from several hundred images (381). We acknowledge the clear-sky bias in LST measurements, and we expect the impact of cloud-based artifacts to be minimized over this long averaging period.

To assign an SUHI value at each pixel, we subtracted a reference rural LST value from the LST at each pixel, where reference rural LST was defined here as corresponding to the median of all LST values from nonwater, 0%-ISA pixels in each seasonal average map. Note that all measurements of LST and SUHI are restricted to the satellite overpass time (~1015 LT), and therefore all discussion of SUHI and LST refers to the daytime effects. To facilitate comparison, discussions of daytime UHI effects on T_a and VPD also focus on the midmorning (1000–1100 LT).

3. Results

a. Temporal variability in UHI intensity

Sensor network measurements suggest strong linear relationships between local ISA and T_a and VPD (Fig. 2). Over 70% of the estimated models were statistically significant (significance level $p < 0.05$), with R^2

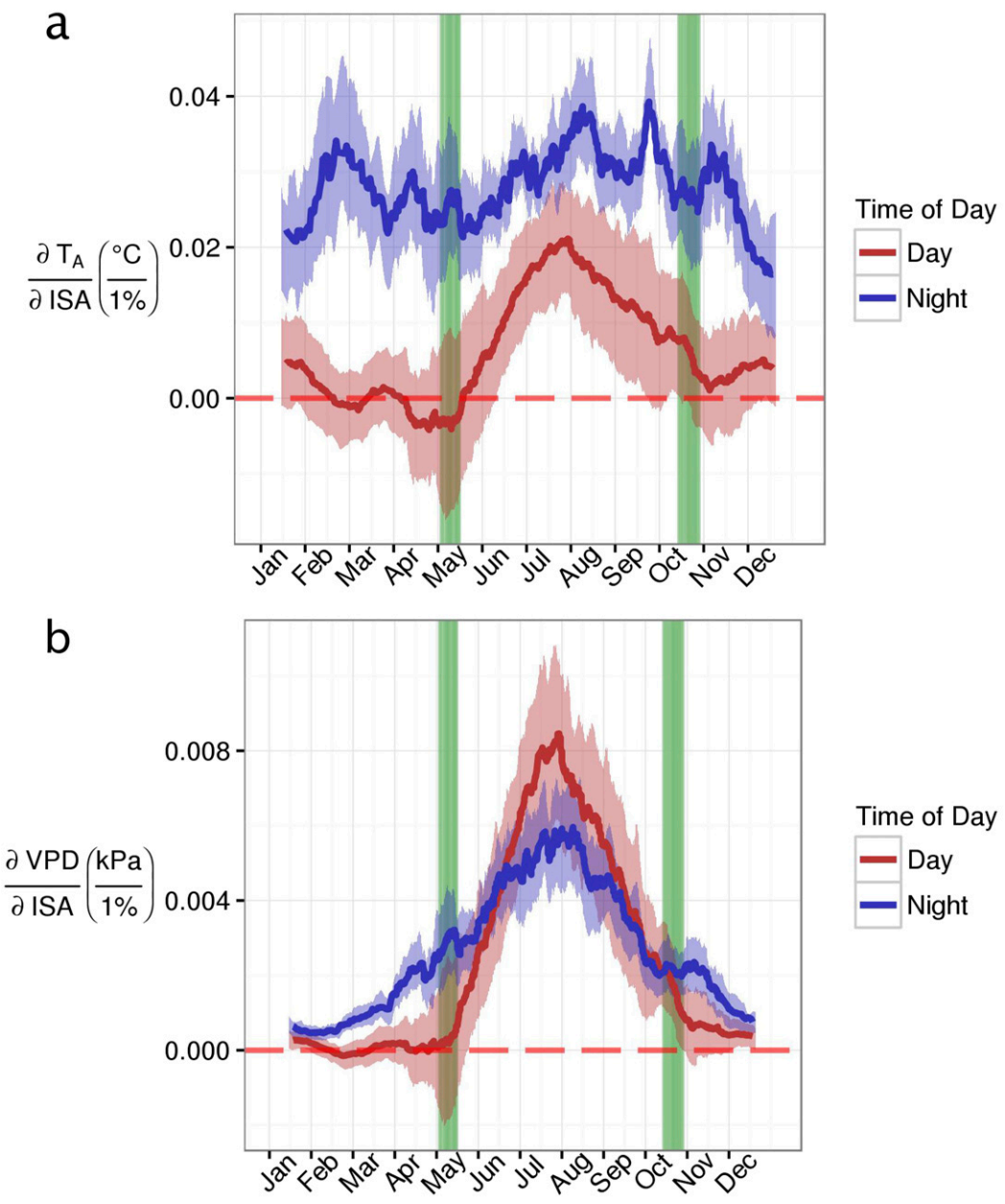

FIG. 3. (a) The 30-day running mean ± 2 std dev (shading) of marginal urban–rural (a) ∂T_a and (b) ∂VPD across the seasonal cycle. Daytime values are in red; nighttime values are in blue. Values are averaged across 2014 and 2015. Vertical green lines indicate the timing of vegetation leaf-out and senescence at each sensor.

varying between 0.5 and 0.75 (Fig. 2). During February of 2015, the average R^2 for VPD briefly dropped to 0.4, when heavy snowfall covered several sensors and insulated them from the atmosphere. Because of the inclement weather associated with the heavy snow, we did not have a means of reliably determining which sensors were affected by snow cover. Thus, it was not feasible to filter these sensors out during the snow-covered period. Our statistical models are estimated for each hour independently; thus, the lower-quality fits from the winter of 2015 do not impact the models in other times of the year.

Multiple-linear-regression results show distinct seasonality in the daytime and nighttime models of urban heating and urban drying. We illustrate the seasonality in ∂T_a and ∂VPD using 30-day running means in Fig. 3. In these plots, nighttime is defined as the period between 0200 and 0500 LT and daytime is defined as the period

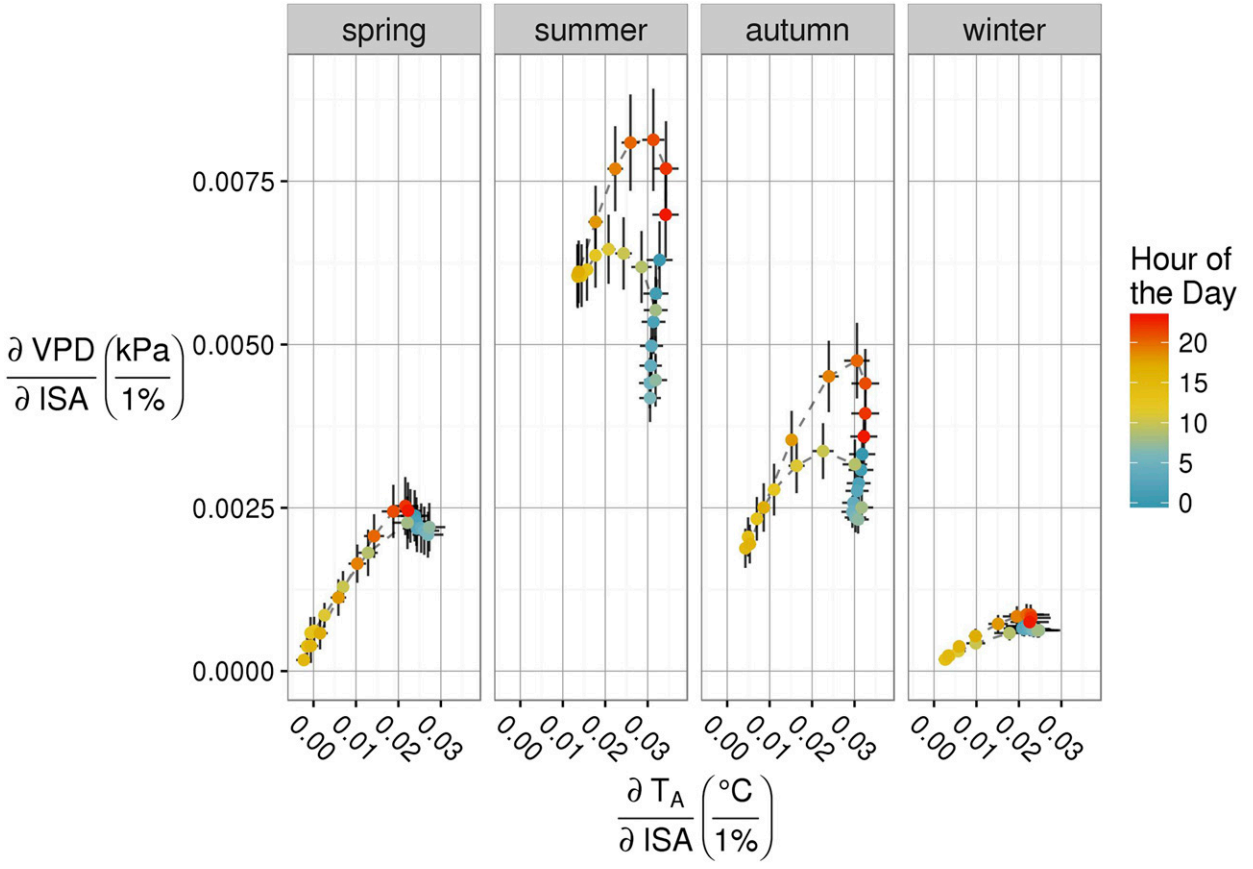

FIG. 4. Diurnal characteristics of marginal urban–rural ∂T_a and ∂VPD, demonstrating a hysteresis behavior for different seasons. Points indicate hourly mean values, and bars indicate ± 2 standard errors. The color of the points indicates the local hour of the day (i.e., morning in blue shades, afternoon in yellow, and evening in red).

between 1200 and 1500 LT. We observed maximum urban heating during nighttime, with ∂T_a varying between 0.02° and 0.04°C per unit ISAover the course of the year, with little seasonality (Fig. 3). In contrast, daytime ∂T_a was strongly seasonal; outside the growing season (i.e., December–March), daytime ∂T_a was near 0.00°C per unit ISA, but it increased during the growing season, peaking at 0.02°C per unit ISA during July–August. Seasonality in daytime ∂T_a appears to be related to the timing of vegetation seasonality, with a sharp increase occurring shortly after leaf-out. These results suggest maximum potential urban–rural differences in T_a attributable to ISA of 0°–2°C during the day and 2°–4°C at night.

The urban drying effect showed strong seasonality in both daytime and nighttime. Daytime ∂VPD remained near 0.0000 kPa per unit ISA outside the growing season but increased sharply after the start of the growing season, peaking at 0.0085 kPa per unit ISA during July–August. Maximum nighttime ∂VPD was 0.006 kPa per unit ISA in July–August and decreased to 0.0005 kPa per unit ISA outside the growing season. During the growing season, daytime ∂VPD was higher than nighttime ∂VPD; the opposite was true outside the growing season. This increase in daytime ∂VPD appears to be strongly related to the timing of vegetation leaf-out, as for ∂T_a; nighttime ∂VPD showed seasonality that was less affected by the timing of leaf-out.

The diurnal cycles of ∂T_a and ∂VPD were highly asymmetric, with distinct variations in growing-season (summer and autumn) and nongrowing-season (spring and winter) diurnal hysteresis (Fig. 4). During spring and winter, the relationships between ∂T_a and ∂VPD are relatively symmetric about the diurnal cycle, with little diurnal hysteresis (Fig. 4). Both ∂T_a and ∂VPD are minimized around nongrowing-season midday (near no effect for both values and for both spring and winter) and reach their maximum around midnight (0.025°C per unit ISA and 0.0025 kPa per unit ISA in spring; 0.025°C per unit ISA and 0.001 kPa per unit ISA in winter). This suggests that increases in urban VPD during these seasons are explained primarily by increases in urban temperature. Diurnal patterns in the relationship between

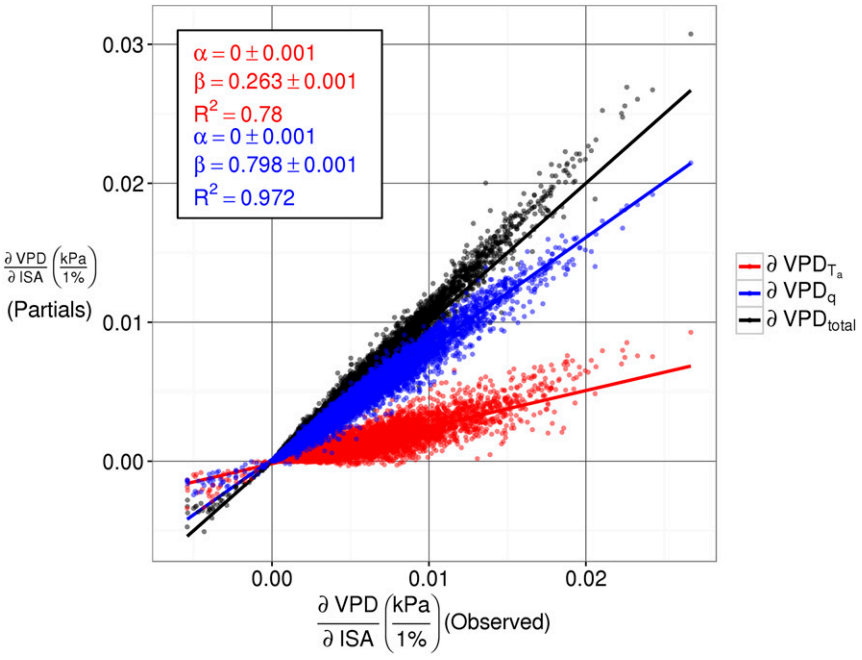

FIG. 5. Relationship between observed marginal urban–rural ∂VPD and ∂VPD_q (in blue) or $\partial\text{VPD}_{\text{Ta}}$ (in red), as well as their sum (labeled $\partial\text{VPD}_{\text{total}}$, in black). On average, ∂VPD_q accounts for ~79% of $\partial\text{VPD}_{\text{total}}$.

∂T_a and ∂VPD during the growing season are highly asymmetric, however, with changes in ∂T_a and ∂VPD decoupled during the night and early–midmorning (Fig. 4). During the night (between 2200 and 0600 LT), ∂T_a is high (0.03°C per unit ISA) and is invariant while ∂VPD drops dramatically from a daily maximum (0.008 kPa per unit ISA in summer; 0.005 kPa per unit ISA in autumn) to a daily minimum (0.0035 kPa per unit ISA in summer; 0.0025 kPa per unit ISA in autumn). After sunrise (~0500 LT), ∂VPD increases rapidly whereas ∂T_a remains high until 0800 LT, after which ∂T_a begins to decline and ∂VPD is relatively invariant at intermediate values (0.006 kPa per unit ISA in summer; 0.002 kPa per unit ISA in autumn). After roughly 1500 LT, ∂VPD and ∂T_a both increase sharply until approximately 2000 LT, when they reach their maximum. Overall, changes in ∂T_a and ∂VPD are decoupled (i.e., changes are asynchronous) during the nighttime and morning (2000–1200 LT) and are coupled (i.e., both values change simultaneously) during the afternoon (1300–1900 LT), which may be related to diurnal changes in vegetation stomatal opening. During the growing season, changes in ∂VPD generally precede changes in ∂T_a, particularly in the early morning.

b. *Attribution of vapor pressure deficit differences*

Changes in vapor pressure deficit can arise from changes in saturation vapor pressure (via changes in temperature) or from changes in the absolute water content. The diurnal asymmetry in ∂T_a and ∂VPD that is shown in Fig. 4 suggests that variability in ∂VPD cannot be explained by variability in ∂T_a alone. Figure 5 shows the relative contributions of changes in temperature and water content in the observed urban–rural VPD differences described by the multiple linear regressions. These results clearly show that total ∂VPD is driven mostly (79%) by urbanization-dependent differences in water content (∂VPD_q). Our results show a slight bias in these estimates in which the sum of the water content and temperature contributions exceeds the observed total dryness by about 6% (i.e., $\partial\text{VPD}_{\text{Ta}} + \partial\text{VPD}_q = 0.799 + 0.263 = 1.057$). As noted above, ∂VPD is very low outside the growing season; therefore most of these relationships represent growing-season ∂VPD. Within the growing season, the relative contribution of ∂VPD_q does not change dramatically (data not shown).

c. *Spatiotemporal variability in urban T_a and VPD*

The estimated linear models reveal considerable spatiotemporal variability in ΔT_a and ΔVPD (Figs. 6 and 7). During the spring daytime, ∂T_a and ∂VPD are minimal [scenewide averages of 0.13° ± 0.15°C and 0.023 ± 0.027 kPa (mean and standard deviation) for ΔT_a and ΔVPD, respectively], implying virtually no modification of surface climate by urban land use. We refer to suburbs as regions where ISA falls between 20% and 80%,

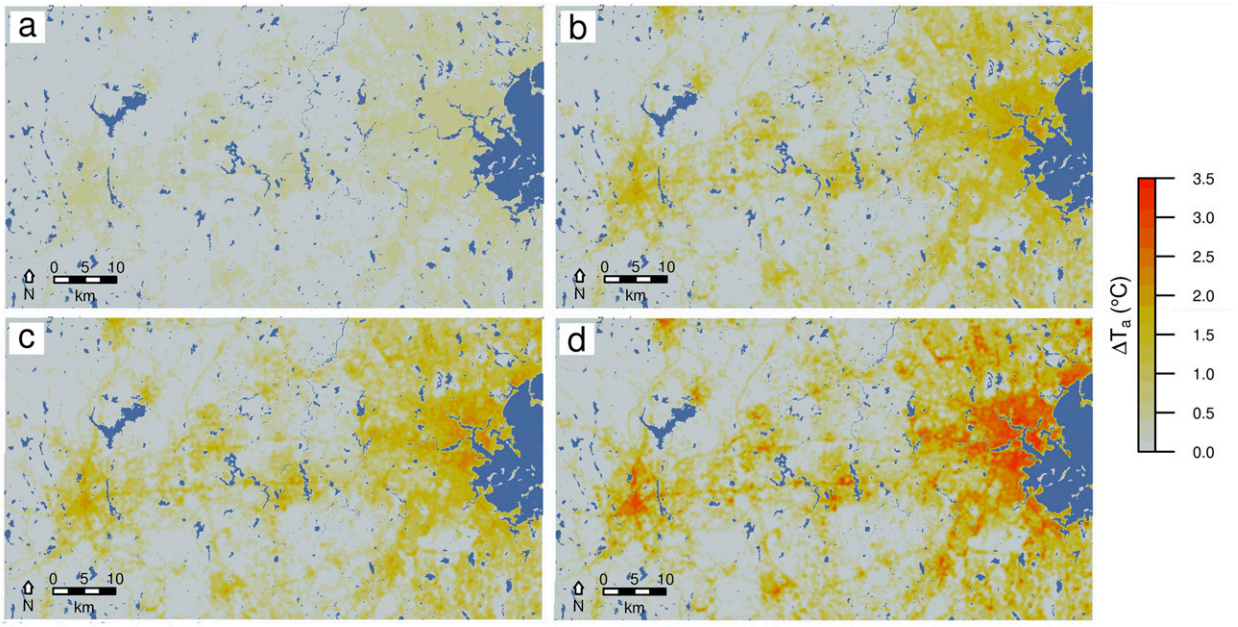

FIG. 6. Maps illustrating the total enhancement in air temperature arising from ISA (ΔT_a) as predicted by linear models. The values given in parentheses in this caption are the mean ± 2 standard errors over all models in each temporal subset. Shown are (a) spring daytime (R^2 = 0.499 ± 0.028; RMSE = 0.512° ± 0.036°C), (b) spring nighttime (R^2 = 0.674 ± 0.034; RMSE = 0.487° ± 0.048°C), (c) summer daytime (R^2 = 0.589 ± 0.028; RMSE = 0.566° ± 0.034°C), and (d) summer nighttime (R^2 = 0.722 ± 0.018; RMSE = 0.515° ± 0.032°C). Daytime corresponds to 1000 LT (for comparison with the SUHI maps, in Fig. 9 below), and nighttime corresponds to 0000 LT. Note that the scales are constant across time of day and season.

whereas urban cores are areas where ISA is greater than 80%. Rural areas (ISA < 20%), by definition, have limited urban heating effects, based on our linear models. Nighttime ∂T_a during spring is higher, resulting in a moderately elevated ΔT_a of 1.01° ± 0.22°C in the suburbs and 1.90° ± 0.09°C in the urban cores. Spring nighttime ∂VPD is very low (Fig. 4), resulting in a suburban ΔVPD of 0.12 ± 0.02 kPa in the suburbs and ΔVPD of 0.21 ± 0.01 kPa in the urban cores.

During summer, ∂T_a and ∂VPD are considerably higher, resulting in much stronger landscape-scale variability in ΔT_a and ΔVPD (Figs. 6 and 7). Summertime ΔVPD reaches 0.60 ± 0.03 kPa in the urban cores of Boston and Worcester at night, with comparable values (0.54 ± 0.03 kPa) during the daytime. Summer ΔT_a reaches 2.07° ± 0.10°C in the urban cores in the daytime but is considerably larger during the nighttime, with ΔT_a reaching up to 2.91° ± 0.14°C. At intermediate levels of urbanization, model results show substantial variability. Suburban areas and road networks in the region exhibit moderate levels of ΔT_a and ΔVPD; during the summer nights, suburban regions experienced ΔT_a and ΔVPD of 1.67° ± 0.34°C and 0.34 ± 0.07 kPa enhancements, respectively. Summer daytime effects for ΔT_a were 1.19° ± 0.24°C in the suburbs and 2.07° ± 0.10°C in the urban cores. For ΔVPD, summer daytime effects were 0.31 ± 0.06 kPa in the suburbs and 0.54 ± 0.03 kPa in the urban cores. In contrast with ΔT_a, which was more sensitive to the time of day, ΔVPD appears to be much more sensitive to season.

d. *Comparison of air temperature and land surface temperature*

Land surface temperatures, point sampled at the time of measurement from the pixel surrounding each sensor (sample size of 71), were consistently and substantially higher than measured air temperature (Fig. 8). Note that the satellite data only record LST at the overpass time, approximately 1015 LT. The difference between LST and T_a varied with season and underlying ISA, with the largest differences (5°–18°C) occurring during spring and summer, moderate differences (5°–11°C) occurring during autumn, and modest differences (0°–3°C) occurring during winter. The differences between LST and T_a were highest at sensors in locations with high levels of ISA (>80%), with LST–T_a differences reaching 15°C during spring and summer, 10°C in autumn, and 7°C in winter. There was little variation in the LST–T_a difference across lower levels of ISA (<80%), with differences near 10°C in spring and summer, 8°C in autumn, and nearly 0°C in winter.

Maps of the daytime SUHI show substantial spatial heterogeneity and relatively high absolute magnitude in

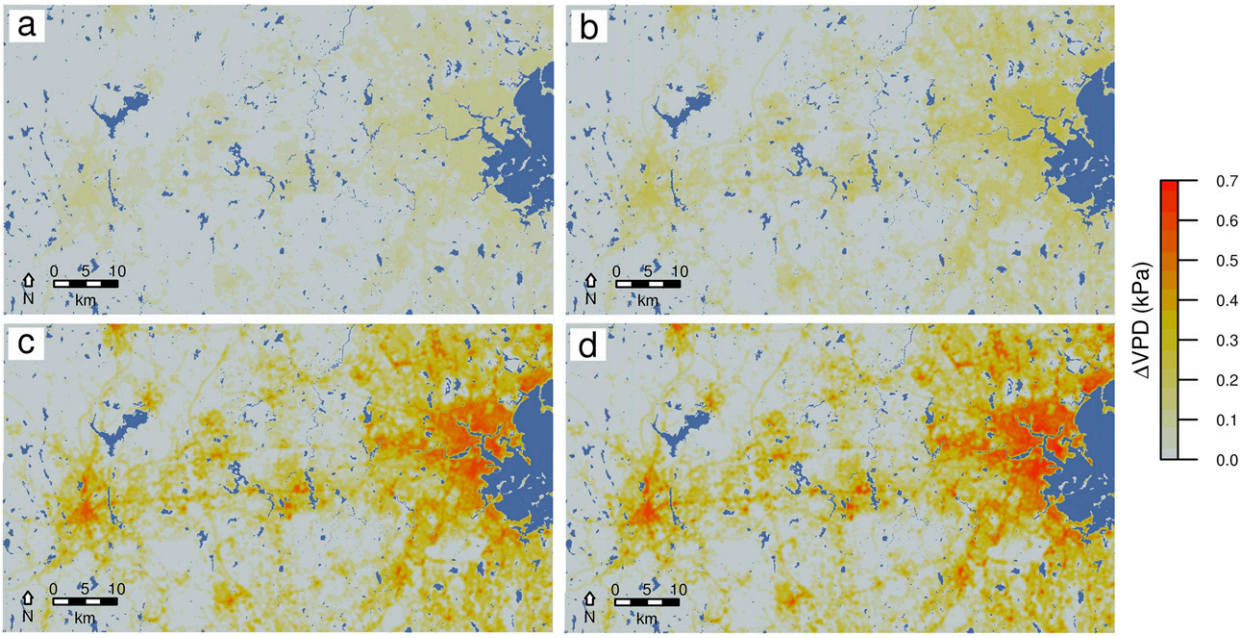

FIG. 7. As in Fig. 6, but for ΔVPD: (a) spring daytime (R^2 = 0.467 ± 0.044; RMSE = 0.0554 ± 0.0068 kPa), (b) spring nighttime (R^2 = 0.629 ± 0.028; RMSE = 0.0526 ± 0.0070 kPa), (c) summer daytime (R^2 = 0.597 ± 0.020; RMSE = 0.1148 ± 0.0082 kPa), and (d) summer nighttime (R^2 = 0.6965 ± 0.018; RMSE = 0.104 ± 0.0078 kPa).

urban–rural differences of LST. On the basis of linear regressions between ISA and LST (R^2 = 0.50 for spring and 0.74 for summer), the effect of the daytime SUHI is 0.062°C per unit ISA during spring and 0.160°C per unit ISA in summer. This is equivalent to a potential maximum range of LST resulting from ISA (ΔLST) of 6.2°C in spring and 16.04°C in summer—values that are substantially higher than the UHI enhancements observed for air temperature in the summer and spring daytimes (ΔT_a = 2.07° ± 0.10°C and 0.12° ± 0.15°C, respectively). This increased range can be seen in the SUHI maps shown in Fig. 9. The SUHI is much less pronounced in spring, with little clearly discernible spatial pattern and SUHI values ranging from −5° to 5°C (Fig. 9). In summer, the SUHI exhibits considerable spatial variability, with the SUHI ranging from 0° to 15°C and noticeable LST "hotspots" corresponding to the urban cores of Boston and Worcester, where the daytime SUHI reached 18°C. Note that our SUHI maps have not been corrected for elevation, distance from ocean, or other exogenous controls, as in the T_a and VPD analyses.

4. Discussion

In this study, we used ISA as the primary land surface parameter to describe the effects of urbanization on surface climates. Our results confirm a strong dependence of UHIs measured by both remote sensing (Yuan and Bauer 2007) and in situ sensor networks (Schatz and Kucharik 2014) on ISA. Urban heating and urban drying both depend on ISA, resulting in significant spatial variability in temperature and dryness. The ΔT_a and ΔVPD maps reflect this spatial variability (Figs. 6 and 7), suggesting that UHI effects are reduced in suburban areas relative to more densely urban areas. As a result, we suggest that studies of UHI will be highly sensitive to the specific locations of sensors or the description of the land cover. We did not consider how other processes, such as trapping of solar radiation, greater retention of outgoing longwave radiation in street canyons, greater heat storage capacity by urban buildings, and the direct release of energy and moisture related to combustion and human metabolism, affect the spatiotemporal variability of T_a, LST, and VPD (Oke 1982; Stewart and Oke 2012). We assume that many of these urban features are correlated with ISA (e.g., more built areas have high population density and tall buildings), and so ISA indirectly captures these effects. Most important is that ISA is negatively correlated with vegetation cover, which drives many of the processes we observe. Future studies might include building height to assess the effect of street canyons (e.g., from lidar or radar remote sensing) and heat storage or diurnally and spatially varying traffic-flow patterns (Gately et al. 2015), but these effects were beyond the scope of this work.

Furthermore, we note that there are a number of open bodies of water in our study area (Fig. 1). Given our

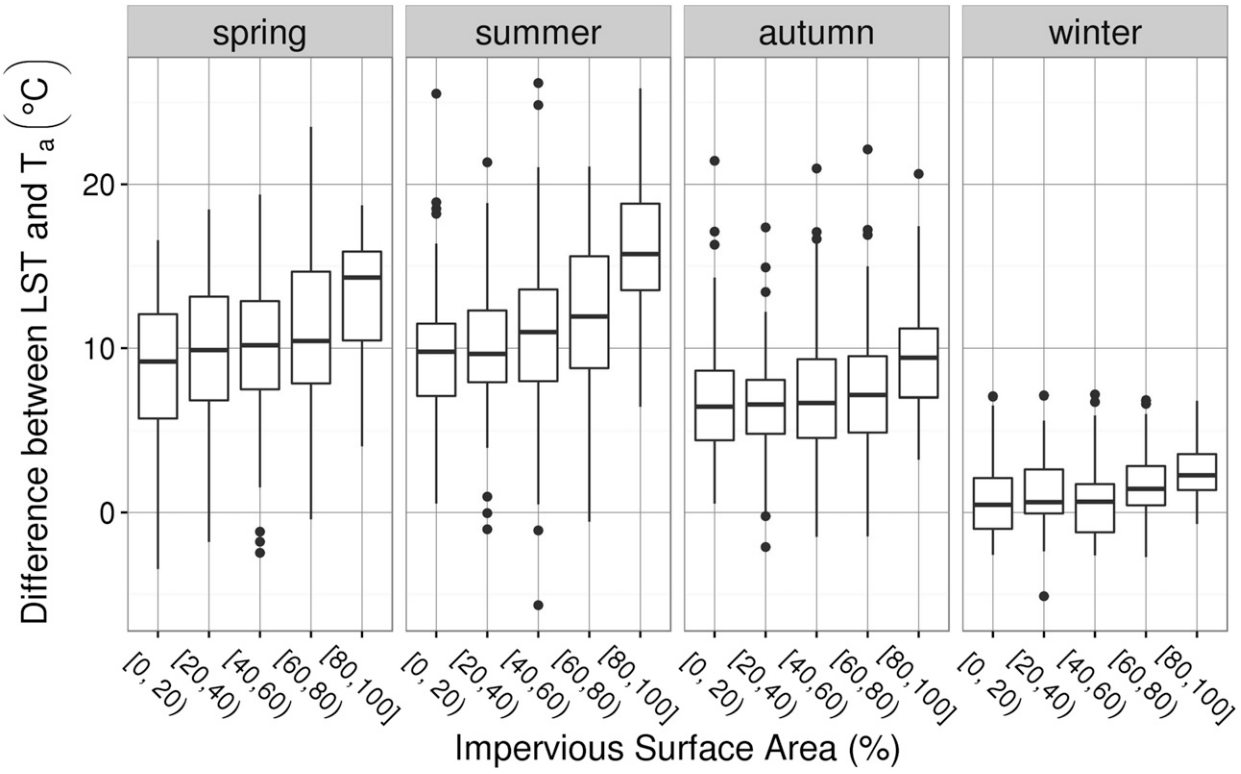

FIG. 8. Seasonal variability in coupling between LST and T_a as a function of ISA. The T_a values correspond to measurements taken at 1000 LT to roughly match the overpass time of Landsat (sample size = 71). Boxes indicate the interquartile range, horizontal bars indicate medians, and whiskers indicate the 10th and 90th percentiles for the difference between LST and T_a for each ISA class and season.

assertion that differences in evaporative cooling rates drive urban heating effects, it would be intuitive that water bodies are likely to have an impact on nearby locations' local atmospheric temperature and humidity. Our analysis has shown that surface climate is significantly controlled by highly local land-cover characteristics, however. It is possible that the water bodies provide a seasonally independent cooling or humidifying effect, particularly on days with higher winds that might cross such water bodies, but we expect these effects to be relatively weak and short ranged. As such, given the relatively limited area of standing water, it is beyond the scope of this paper to quantify the impact of these water bodies on urban surface climate.

Previous studies of urban–rural differences in humidity have shown conflicting results in terms of both direction and magnitude. Some studies suggest seasonally and diurnally dependent humidification of urban environments (Ackerman 1987; Lee 1991; Deosthali 2000; Unkašević et al. 2001), in which urban areas become more humid than rural areas at certain times and less humid at others. Others suggest that urban areas are consistently more humid (Unger 1999; Kuttler et al. 2007) or drier (Jáuregui and Tejeda 1997) throughout the year. Our study suggests that Boston is generally drier than nearby forests across both diurnal and seasonal time scales but that the magnitude of the enhanced dryness varies by season and time of day. Since the seasonality of ∂VPD is related to the seasonality of green-leaf phenology, our results suggest a significant role for vegetation in modifying local moisture content of the urban near-surface atmosphere.

Results from this work are consistent with those from previous studies showing UHIs to be stronger during the nighttime than during the daytime (Gedzelman et al. 2003; Kolokotroni and Giridharan 2008; Yang et al. 2013; Schatz and Kucharik 2014), which is likely caused by increased daytime ground heat storage and increased emission of longwave radiation at night. Our results also show that seasonality in nighttime ∂T_a is low relative to seasonality in daytime ∂T_a, which suggests that regional differences in evapotranspiration between urban and rural areas at least partly explain this pattern. We propose an ecophysiological explanation for the reported results: As leaves emerge in spring, transpiration by forests humidifies the lower atmosphere of rural areas, whereas in urban areas lower vegetative cover and higher ISA lead to reduced rates of transpiration and lower humidity.

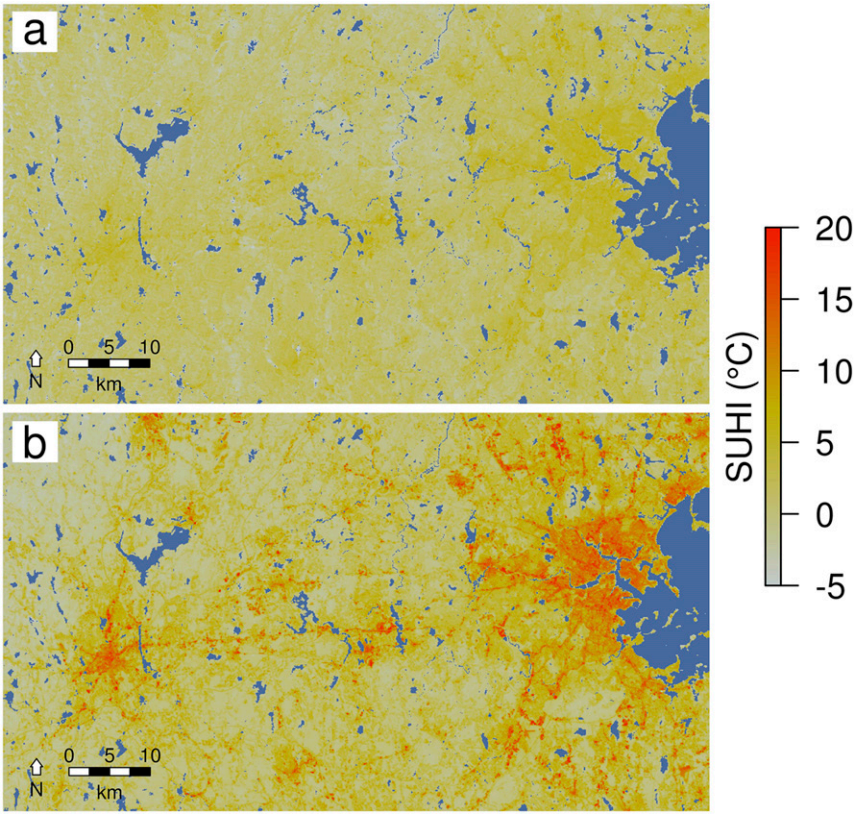

FIG. 9. Maps illustrating the SUHI as inferred from Landsat LST data for (a) spring and (b) summer. The Landsat overpass time is ~1015 local time; hence, these maps illustrate the midmorning SUHI. The LST data were averaged across each season and normalized relative to the median LST value for 0%-ISA, nonwater pixels. Note that the magnitude of the SUHI is considerably higher than the air temperature enhancement that is seen in Figs. 6 and 7.

During the daytime, rural areas with higher vegetation density have higher rates of evapotranspiration and lower Bowen ratios, which situation acts to cool and humidify the atmosphere relative to urban areas. During nighttime, no photosynthesis or transpiration occurs, reducing the impact of vegetation seasonality. This explanation, however, is complicated by the fact that urban vegetation is often actively irrigated and fertilized and thus experiences human management in its ecophysiological status. Further, urban–rural differences in species composition may influence the ecophysiological explanation, particularly considering potentially complex interactions between human management in urban biodiversity and bioclimatic filtering (Jenerette et al. 2016).

As we mentioned above, results suggest that urban trees actively modify the local humidity of the lower atmosphere. Diurnal hysteresis between ∂T_a and ∂VPD shows that ∂VPD generally preceded changes in ∂T, suggesting potential causality between ∂VPD and ∂T_a that underlies their asynchronous variability. The fact that ∂VPD is driven mostly by changes in atmospheric water content further supports a feedback mechanism between vegetation and urban humidity. Because water vapor stress can induce stomatal closure and reduced transpiration, this mechanism has the potential to create a positive feedback loop that leads to higher stress in sparsely vegetated patches than in more densely vegetated patches. This is supported by the hysteresis between ∂T_a and ∂VPD, which shows that the ∂VPD stabilizes somewhat in the middle of the day but rapidly increases in the afternoon when urban vegetation can no longer buffer near-surface atmospheric water content, after which ∂T_a also increases. It is at this point that urban temperatures begin to rise, further raising VPD via increased evaporative demand and stomatal closure. At the same time, urban–rural differences in VPD are at a minimum at night, when no photosynthesis occurs, all stomata are closed, and transpiration rates are near 0 for both urban and rural areas. This suggests that changes in daytime UHI intensity are mediated by vegetation-driven transpiration via changes in VPD gradients on hourly time scales, whereas nighttime UHI

effects are less affected by differences in rates of transpiration. This connection reinforces the role of spatial variation in green-leaf phenology and evapotranspiration as a key driver of urban-to-rural differences in surface climate. Considering the evidence that UHIs have significant impacts on urban vegetation phenology through changes in temperature (Zhang et al. 2004; Jochner and Menzel 2015; Melaas et al. 2016) and the potential for tree phenology to be sensitive to local humidity (Laube et al. 2014), this interaction would imply significant potential feedbacks between the timing of leaf phenology and the mediation of urban climate by vegetation.

The impact of urbanization on surface air temperature differs significantly from the impact on land surface temperature. It is well established that LST is typically higher than T_a during daytime, and previous studies have found significant differences in the ability of LST to predict T_a between nighttime and daytime, suggesting that the microclimatic and biophysical mechanisms that affect LST–T_a coupling is still relatively unclear (Oyler et al. 2016). We show here that the degree to which LST and T_a are coupled also depends on the amount of ISA and the season. Our results suggest a nonlinear relationship between LST and T_a that depends on ISA, potentially biasing analyses that take the SUHI as a surrogate for air UHI. The nonlinear coupling between LST and T_a suggests that gradients in temperature between the surface and the air will be higher than expected in densely urbanized landscapes. More important is that temporal variability in coupling between LST and T_a suggests that using remotely sensed SUHI as a surrogate for UHIs may lead to biases if seasonality in the SUHI effect is not directly addressed. The drivers behind both phenomena are similar, resulting in fairly similar spatial patterns, but it is important to understand the nature, magnitude, and seasonality in differences between the two phenomena.

5. Conclusions

Most urban surface climate studies focus on either temporal variability (i.e., bulk differences between urban and rural temperatures) or spatial variability (e.g., via land surface temperature images from remote sensing) in urban temperatures. In this study, we explored the factors that control spatial *and* temporal variation in T_a and VPD and showed that the magnitude of urban–rural gradients in air temperature and vapor pressure deficit in Boston depend jointly on time of day, time of year, vegetation cover, and local urban land use. To be more specific, our results show that diurnal and seasonal variations in Boston's urban heat island are strongly controlled by ISA and that both the magnitude and coupling of urban-to-rural gradients in VPD and T_a depend on the seasonality of local vegetation cover. We also observed clear diurnal hysteresis in the relationship between VPD and T_a, where changes in VPD gradients preceded changes in T_a gradients, which suggests that daytime UHI intensity is mediated by vegetation-driven transpiration that is at least partly caused by short-term changes in local VPD. As a result, the amount and seasonality of vegetation at any location exerted strong influence on the local magnitude of urban–rural differences in VPD and T_a and on the strength of coupling between T_a and LST.

Our study examined only one metropolitan area, and the nature and magnitude of UHIs and the relationships we explore in this paper can vary substantially across bioclimatic zones, especially across those with different vegetation types. Because the presence of vegetation strongly influences urban microclimates, it follows that cities with different vegetation cover than Boston's (e.g., those located in more arid or in boreal climate regimes) will exhibit urban microclimatic controls and patterns that differ from those we observed in Boston. In addition, cities vary widely in their structure, zoning, and land-use management, all of which add further spatiotemporal complexity to surface climates in cities. Hence, while the patterns and results we present in this paper are probably representative of urban microclimates in temperate North American cities, more research is required to better understand how applicable the results and conclusions we draw from this work are to cities that are located in different climate zones or in countries that are less developed economically or that have different approaches to urban planning.

The maps of ΔT_a, ΔVPD, and SUHI presented in this paper illustrate that there was substantial spatial and temporal variability in T_a, VPD, and LST in the Boston metropolitan area, which suggests that characterization of urban microclimates on the basis only of bulk urban–rural differences is not sufficient to fully understand how surface properties control urban microclimates. The impervious surface area controls the spatial variability in urban climatic effects, whereas the vegetation controls the temporal variability; the societal impacts of UHI are also likely to vary spatially and temporally with ISA and vegetation seasonality. In the coming decades, urban areas worldwide are expected to grow significantly in terms of both the land area they occupy and their populations. Hence, understanding how urban land-use affects surface climate has important implications for energy use (i.e., air conditioning), public health, and, in a more broad sense, the role and contribution of cities to regional climate change.

Acknowledgments. We thank Steve Raciti and Jackie Getson-Hardiman for their assistance in planning and deploying the sensor network. We thank Alison Dunn,

Peter Del Tredici, and many others for graciously hosting our sensor network on their property. This work was supported by NASA Grants NNX12AM82G and NNX14AI70G and by a National Science Foundation Graduate Research Fellowship (Grant DGE-1247312).

REFERENCES

Ackerman, B., 1987: Climatology of Chicago area urban–rural differences in humidity. *J. Climate Appl. Meteor.*, **26**, 427–430, doi:10.1175/1520-0450(1987)026<0427:COCAUR>2.0.CO;2.

Alcoforado, M.-J., and H. Andrade, 2006: Nocturnal urban heat island in Lisbon (Portugal): Main features and modelling attempts. *Theor. Appl. Climatol.*, **84**, 151–159, doi:10.1007/s00704-005-0152-1.

Arnfield, A. J., 2003: Two decades of urban climate research: A review of turbulence, exchanges of energy and water, and the urban heat island. *Int. J. Climatol.*, **23**, 1–26, doi:10.1002/joc.859.

Auer, A. H., Jr., 1978: Correlation of land use and cover with meteorological anomalies. *J. Appl. Meteor.*, **17**, 636–643, doi:10.1175/1520-0450(1978)017<0636:COLUAC>2.0.CO;2.

Barsi, J. A., J. R. Schott, F. D. Palluconi, and S. J. Hook, 2005: Validation of a web-based atmospheric correction tool for single thermal band instruments. *Earth Observing Systems X*, J. J. Butler, Ed., International Society for Optical Engineering (SPIE Proceedings, Vol. 5882), 58820E, doi:10.1117/12.619990.

Bounoua, L., and Coauthors, 2015: Impact of urbanization on US surface climate. *Environ. Res. Lett.*, **10**, 084010, doi:10.1088/1748-9326/10/8/084010.

Bowler, D. E., L. Buyung-Ali, T. M. Knight, and A. S. Pullin, 2010: Urban greening to cool towns and cities: A systematic review of the empirical evidence. *Landscape Urban Plann.*, **97**, 147–155, doi:10.1016/j.landurbplan.2010.05.006.

Briber, B. M., L. R. Hutyra, A. B. Reinmann, S. M. Raciti, V. K. Dearborn, C. E. Holden, and A. L. Dunn, 2015: Tree productivity enhanced with conversion from forest to urban land covers. *PLoS One*, **10**, e0136237, doi:10.1371/journal.pone.0136237.

Deosthali, V., 2000: Impact of rapid urban growth on heat and moisture islands in Pune City, India. *Atmos. Environ.*, **34**, 2745–2754, doi:10.1016/S1352-2310(99)00370-2.

Diao, M., M. A. Zondlo, A. J. Heymsfield, L. M. Avallone, M. E. Paige, S. P. Beaton, T. Campos, and D. C. Rogers, 2014: Cloud-scale ice-supersaturated regions spatially correlate with high water vapor heterogeneities. *Atmos. Chem. Phys.*, **14**, 2639–2656, doi:10.5194/acp-14-2639-2014.

Eliasson, I., and M. K. Svensson, 2003: Spatial air temperature variations and urban land use—A statistical approach. *Meteor. Appl.*, **10**, 135–149, doi:10.1017/S1350482703002056.

Ellefsen, R., 1991: Mapping and measuring buildings in the canopy boundary layer in ten U.S. cities. *Energy Build.*, **16**, 1025–1049, doi:10.1016/0378-7788(91)90097-M.

Friedl, M. A., J. M. Gray, E. K. Melaas, A. D. Richardson, K. Hufkens, T. F. Keenan, A. Bailey, and J. O'Keefe, 2014: A tale of two springs: Using recent climate anomalies to characterize the sensitivity of temperate forest phenology to climate change. *Environ. Res. Lett.*, **9**, 054006, doi:10.1088/1748-9326/9/5/054006.

Gately, C. K., L. R. Hutyra, and I. S. Wing, 2015: Cities, traffic, and CO_2: A multidecadal assessment of trends, drivers, and scaling relationships. *Proc. Natl. Acad. Sci. USA*, **112**, 4999–5004, doi:10.1073/pnas.1421723112.

Gedzelman, S. D., S. Austin, R. Cermak, N. Stefano, S. Partridge, S. Quesenberry, and D. A. Robinson, 2003: Mesoscale aspects of the urban heat island around New York City. *Theor. Appl. Climatol.*, **75**, 29–42, doi:10.1007/s00704-002-0724-2.

Georgescu, M., P. E. Morefield, B. G. Bierwagen, and C. P. Weaver, 2014: Urban adaptation can roll back warming of emerging megapolitan regions. *Proc. Natl. Acad. Sci. USA*, **111**, 2909–2914, doi:10.1073/pnas.1322280111.

Grossman-Clarke, S., J. A. Zehnder, T. Loridan, and C. S. B. Grimmond, 2010: Contribution of land use changes to near-surface air temperatures during recent summer extreme heat events in the Phoenix metropolitan area. *J. Appl. Meteor. Climatol.*, **49**, 1649–1664, doi:10.1175/2010JAMC2362.1.

Hage, K. D., 1975: Urban–rural humidity differences. *J. Appl. Meteor.*, **14**, 1277–1283, doi:10.1175/1520-0450(1975)014<1277:URHD>2.0.CO;2.

Hinkel, K. M., and F. E. Nelson, 2007: Anthropogenic heat island at Barrow, Alaska, during winter: 2001–2005. *J. Geophys. Res.*, **112**, D06118, doi:10.1029/2006JD007837.

Hjort, J., J. Suomi, and J. Käyhkö, 2011: Spatial prediction of urban–rural temperatures using statistical methods. *Theor. Appl. Climatol.*, **106**, 139–152, doi:10.1007/s00704-011-0425-9.

——, ——, and ——, 2016: Extreme urban–rural temperatures in the coastal city of Turku, Finland: Quantification and visualization based on a generalized additive model. *Sci. Total Environ.*, **569–570**, 507–517, doi:10.1016/j.scitotenv.2016.06.136.

Homer, C. G., and Coauthors, 2015: Completion of the 2011 National Land Cover Database for the conterminous United States—Representing a decade of land cover change information. *Photogramm. Eng. Remote Sens.*, **81**, 345–354. [Available online at http://www.sciencedirect.com/science/article/pii/S0099111215301002.]

Imhoff, M. L., P. Zhang, R. E. Wolfe, and L. Bounoua, 2010: Remote sensing of the urban heat island effect across biomes in the continental USA. *Remote Sens. Environ.*, **114**, 504–513, doi:10.1016/j.rse.2009.10.008.

Jáuregui, E., and A. Tejeda, 1997: Urban–rural humidity contrasts in Mexico City. *Int. J. Climatol.*, **17**, 187–196, doi:10.1002/(SICI)1097-0088(199702)17:2<187::AID-JOC114>3.0.CO;2-P.

Jenerette, G. D., and Coauthors, 2016: Climate tolerances and trait choices shape continental patterns of urban tree biodiversity. *Global Ecol. Biogeogr.*, **25**, 1367–1376, doi:10.1111/geb.12499.

Jochner, S., and A. Menzel, 2015: Urban phenological studies—Past, present, future. *Environ. Pollut.*, **203**, 250–261, doi:10.1016/j.envpol.2015.01.003.

Kim, Y.-H., and J.-J. Baik, 2005: Spatial and temporal structure of the urban heat island in Seoul. *J. Appl. Meteor.*, **44**, 591–605, doi:10.1175/JAM2226.1.

Kolokotroni, M., and R. Giridharan, 2008: Urban heat island intensity in London: An investigation of the impact of physical characteristics on changes in outdoor air temperature during summer. *Sol. Energy*, **82**, 986–998, doi:10.1016/j.solener.2008.05.004.

Kuttler, W., S. Weber, J. Schonnefeld, and A. Hesselschwerdt, 2007: Urban/rural atmospheric water vapour pressure differences and urban moisture excess in Krefeld, Germany. *Int. J. Climatol.*, **27**, 2005–2015, doi:10.1002/joc.1558.

Laube, J., T. H. Sparks, N. Estrella, and A. Menzel, 2014: Does humidity trigger tree phenology? Proposal for an air humidity based framework for bud development in spring. *New Phytol.*, **202**, 350–355, doi:10.1111/nph.12680.

Lee, D. O., 1991: Urban—rural humidity differences in London. *Int. J. Climatol.*, **11**, 577–582, doi:10.1002/joc.3370110509.

Li, D., and E. Bou-Zeid, 2013: Synergistic interactions between urban heat islands and heat waves: The impact in cities is

larger than the sum of its parts. *J. Appl. Meteor. Climatol.*, **52**, 2051–2064, doi:10.1175/JAMC-D-13-02.1.

——, ——, and M. Oppenheimer, 2014: The effectiveness of cool and green roofs as urban heat island mitigation strategies. *Environ. Res. Lett.*, **9**, 055002, doi:10.1088/1748-9326/9/5/055002.

Loridan, T., and C. S. B. Grimmond, 2012: Characterization of energy flux partitioning in urban environments: Links with surface seasonal properties. *J. Appl. Meteor. Climatol.*, **51**, 219–241, doi:10.1175/JAMC-D-11-038.1.

Masson, V., 2000: A physically-based scheme for the urban energy budget in atmospheric models. *Bound.-Layer Meteor.*, **94**, 357–397, doi:10.1023/A:1002463829265.

Melaas, E. K., M. A. Friedl, and Z. Zhu, 2013: Detecting interannual variation in deciduous broadleaf forest phenology using Landsat TM/ETM + data. *Remote Sens. Environ.*, **132**, 176–185, doi:10.1016/j.rse.2013.01.011.

——, J. A. Wang, D. L. Miller, and M. A. Friedl, 2016: Interactions between urban vegetation and surface urban heat islands: A case study in the Boston metropolitan region. *Environ. Res. Lett.*, **11**, 054020, doi:10.1088/1748-9326/11/5/054020.

Nowak, D. J., 2006: Institutionalizing urban forestry as a ''biotechnology'' to improve environmental quality. *Urban For. Urban Greening*, **5**, 93–100, doi:10.1016/j.ufug.2006.04.002.

Oke, T. R., 1982: The energetic basis of the urban heat island. *Quart. J. Roy. Meteor. Soc.*, **108**, 1–24, doi:10.1002/qj.49710845502.

——, 2006: Initial guidance to obtain representative meteorological observations at urban sites. WMO Instruments and Observing Methods Rep. WMO/TD 1250, 47 pp. [Available online at https://www.wmo.int/pages/prog/www/IMOP/publications/IOM-81/IOM-81-UrbanMetObs.pdf.]

Onishi, A., X. Cao, T. Ito, F. Shi, and H. Imura, 2010: Evaluating the potential for urban heat-island mitigation by greening parking lots. *Urban For. Urban Greening*, **9**, 323–332, doi:10.1016/j.ufug.2010.06.002.

Oyler, J. W., S. Z. Dobrowski, Z. A. Holden, and S. W. Running, 2016: Remotely sensed land skin temperature as a spatial predictor of air temperature across the conterminous United States. *J. Appl. Meteor. Climatol.*, **55**, 1441–1457, doi:10.1175/JAMC-D-15-0276.1.

Raciti, S. M., L. R. Hutyra, P. Rao, and A. C. Finzi, 2012: Inconsistent definitions of ''urban'' result in different conclusions about the size of urban carbon and nitrogen stocks. *Ecol. Appl.*, **22**, 1015–1035, doi:10.1890/11-1250.1.

Richardson, A. D., A. S. Bailey, E. G. Denny, C. W. Martin, and J. O'Keefe, 2006: Phenology of a northern hardwood forest canopy. *Global Change Biol.*, **12**, 1174–1188, doi:10.1111/j.1365-2486.2006.01164.x.

Schatz, J., and C. J. Kucharik, 2014: Seasonality of the urban heat island effect in Madison, Wisconsin. *J. Appl. Meteor. Climatol.*, **53**, 2371–2386, doi:10.1175/JAMC-D-14-0107.1.

——, and ——, 2015: Urban climate effects on extreme temperatures in Madison, Wisconsin, USA. *Environ. Res. Lett.*, **10**, 094024, doi:10.1088/1748-9326/10/9/094024.

Seto, K. C., B. Güneralp, and L. R. Hutyra, 2012: Global forecasts of urban expansion to 2030 and direct impacts on biodiversity and carbon pools. *Proc. Natl. Acad. Sci. USA*, **109**, 16 083–16 088, doi:10.1073/pnas.1211658109.

Sobrino, J. A., J. C. Jiménez-Muñoz, and L. Paolini, 2004: Land surface temperature retrieval from Landsat TM 5. *Remote Sens. Environ.*, **90**, 434–440, doi:10.1016/j.rse.2004.02.003.

Stewart, I. D., and T. R. Oke, 2012: Local climate zones for urban temperature studies. *Bull. Amer. Meteor. Soc.*, **93**, 1879–1900, doi:10.1175/BAMS-D-11-00019.1.

Unger, J., 1999: Urban–rural air humidity differences in Szeged, Hungary. *Int. J. Climatol.*, **19**, 1509–1515, doi:10.1002/(SICI)1097-0088(19991115)19:13<1509::AID-JOC453>3.0.CO;2-P.

Unkašević, M., O. Jovanović, and T. Popović, 2001: Urban–suburban/rural vapour pressure and relative humidity differences at fixed hours over the area of Belgrade city. *Theor. Appl. Climatol.*, **68**, 67–73, doi:10.1007/s007040170054.

USGS, 2004: Shuttle Radar Topography Mission, 1 arc second scene SRTM_u03_n008e004, Unfilled Unfinished 2.0. University of Maryland Global Land Cover Facility, accessed 10 March 2016. [Available online at http://www.landcover.org/data/srtm/.]

Weng, Q., and P. Fu, 2014: Modeling annual parameters of clear-sky land surface temperature variations and evaluating the impact of cloud cover using time series of Landsat TIR data. *Remote Sens. Environ.*, **140**, 267–278, doi:10.1016/j.rse.2013.09.002.

——, D. Lu, and J. Schubring, 2004: Estimation of land surface temperature–vegetation abundance relationship for urban heat island studies. *Remote Sens. Environ.*, **89**, 467–483, doi:10.1016/j.rse.2003.11.005.

Yang, P., G. Ren, and W. Liu, 2013: Spatial and temporal characteristics of Beijing urban heat island intensity. *J. Appl. Meteor. Climatol.*, **52**, 1803–1816, doi:10.1175/JAMC-D-12-0125.1.

Yuan, F., and M. E. Bauer, 2007: Comparison of impervious surface area and normalized difference vegetation index as indicators of surface urban heat island effects in Landsat imagery. *Remote Sens. Environ.*, **106**, 375–386, doi:10.1016/j.rse.2006.09.003.

Zhang, X., M. A. Friedl, C. B. Schaaf, A. H. Strahler, and A. Schneider, 2004: The footprint of urban climates on vegetation phenology. *Geophys. Res. Lett.*, **31**, L12209, doi:10.1029/2004GL020137.

Zhou, B., D. Rybski, and J. P. Kropp, 2013: On the statistics of urban heat island intensity. *Geophys. Res. Lett.*, **40**, 5486–5491, doi:10.1002/2013GL057320.

Zhu, Z., and C. E. Woodcock, 2012: Object-based cloud and cloud shadow detection in Landsat imagery. *Remote Sens. Environ.*, **118**, 83–94, doi:10.1016/j.rse.2011.10.028.